Chapter-4: Study of Structural-Electrical……

4.1 Introduction

It has been reported that the conductivity of pure LAO is less than that of YSZ. Ion dynamics of LAO have been discussed in chapter 3. Also, it has been reported that the electrolyte material, satisfying all the conditions, conduction is generally depends on the concentration of defects. The ionic conductivity can be raised by alio-valent co-substitution(s), which in turn increase the concentration of ionic defect. Further enhancement of conductivity has been reported by double substitution. Due to perovskite structure of LAO, it has generally stable crystal structure, large free lattice volume and substitution liberty.

The prime requisite in the fabrication of electrolyte systems is high oxide ion conductivity with no porosity or less porosity. Moreover, it should be as thin as possible so that the ohmic loss is reduced. For this purpose, casting of thin tape of the electrolyte is essential. The efficiency depends on the properties of thin tape. Amongst various techniques, tape casting is a good method to produce thin, flat and large area ceramic tape with a thickness range of 0.1-1000 μm. With reference to other conventional ceramic procedures, tape casting is a low cost ceramic fabrication technique, which produced wide and thin ceramic tapes having precise dimensional tolerances and very smooth surfaces. It is also observed that tape casting leads to a very homogenous microstructure and is a well-established procedure at large scale fabrication of ceramic substrates and multilayered structures. It is reported that various authors used different methods of tape casting techniques. Chin Myung Whang at al. used chemical solution deposition method for thin film of YSZ electrolyte for intermediate temperature SOFCs [79]. Thomas Ryll at al. used spray pyrolysis method for lanthanum nickelate thin films. Xinzhi Chen at al.

prepared $La_2NiO_{4+\delta}$ by aqueous tape casting method[80]. Ming Zhang at al. prepared solid state lithium ionic conducting thin film $Li_{1.4}Al_{0.4}Ge_{1.6}(PO_4)_3$ by tape casting method [81]. Xuewei Ba used transparent $Y_3Al_5O_{12}$ ceramics produced by an aqueous tape casting method.

In this chapter, the systematic study with co-substitution and double substitution on LAO based systems have been done. Here, it is defined co-substitution as simultaneous equi-molar substitution at A-site and B-site of perovskite while, double substitution is defined as further substitution at A-site in traces.

This chapter is divided into two parts: first, It has been studied the structure and conductivity and tried to establish a correlation between them and second, it has been planned to prepare a thin tape of $(La_{0.89}\ Ba_{0.01})\ Sr_{0.1}Al_{0.9}Mg_{0.1}O_{3-\delta}$ by the tape casting technique and investigate its structural and electrical properties. Further, we have compared the structural and electrical properties of both the pellet and the tape synthesized.

4.2 Doping Strategy

In co-substitution, first 'Sr' doped on the La-site and 'Mg' doped on the Al - site of LAO to get the composition $(Sr_{0.1}La_{0.9})(Mg_{0.1}Al_{0.9})O_3$ (abbr. as LSAM or B0) as reported that the solubility limit of Sr^{2+} and Mg^{2+} was 10% for better ionic conductivity. Subsequently, it has been prepared a double substituted system with the substitution of 'Ba' on the La site. The perovskite oxides are generally possessing oxygen vacancies, which further increases with aliovalent substitution; thus concentration of oxygen vacancies can be altered [29]. The defect equations can estimate the number of oxygen vacancy generated with the substitutions and it can be written as (using Kroger -Vink notation):

With strontium oxide and Magnesium substitution:

$$SrO + MgO \xrightarrow{LaAlO3} Sr'_{La} + Mg'_{Al} + 2O_o + V^{\bullet\bullet}$$

With additional barium oxide substitution:

$$2BaO + Al_2O_3 \xrightarrow{2xLaAlO_3} 2Ba'_{La} + 2Al^{\times}{}_{Al} + 5O_o + V^{\bullet\bullet}$$

The overall equation can be summed together as,

$$2xBaO + 0.1SrO + 0.1MgO + xAl_2O_3 \xrightarrow{(0.1+2x)LaAlO_3} 2xBa'_{La} + 2xAl^{\times}{}_{Al} + 0.1Sr'_{La} + 0.1Mg'_{Al} + (0.2+5x)O_o + (0.1+x)V^{\bullet\bullet}$$

We have double substituted Ba with x = 0.01, 0.03, 0.05 and 0.07 in the system $La_{0.9-x}Sr_{0.1}Al_{0.9}Mg_{0.1}O_{3-\delta}$. The samples, hereafter, abbreviated as B0 for 0%, B1 for 1%, B3 for 3%, and B5 for 5% substituted Ba respectively. The Goldschmidt tolerance factor given in Eq. 1.14 has been calculated for these sample (Fig. 4.1). It is found that the tolerance factor is increasing with Ba substitution and structure gets stabilized.

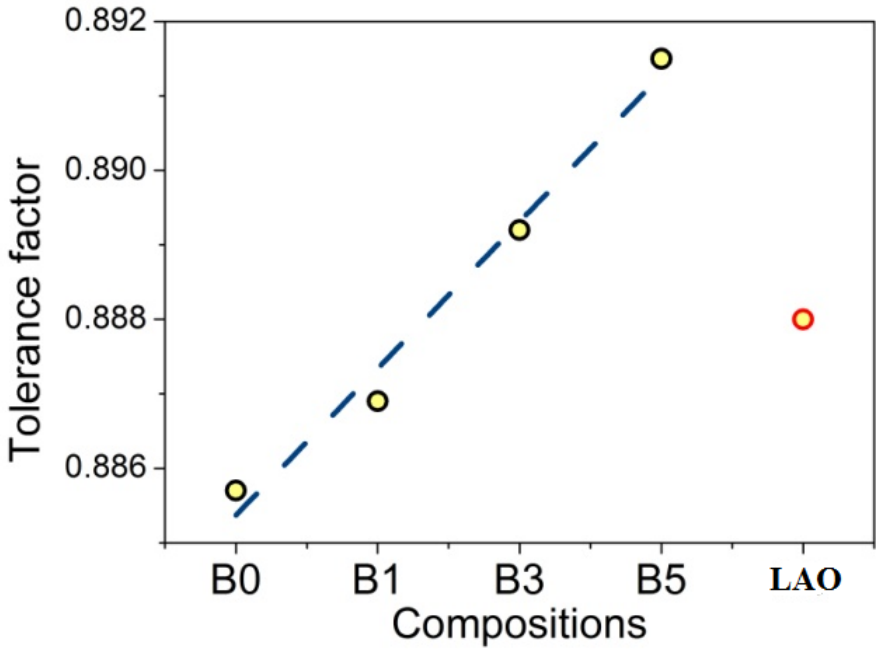

Figure 4.1: Tolerance factor of Ba modified $La_{0.9}Sr_{0.1}Al_{0.9}Mg_{0.1}O_{3-\delta}$ (LSAM) (abbreviation: B0 for 0%, B1 for 1%, B3 for 3%, B5 for 5% substituted Ba respectively and LAO for $LaAlO_3$)

4.3 Experimental

The system $La_{0.9-x}Sr_{0.1}Ba_x\ Al_{0.9}Mg_{0.1}O_{3-\delta}$, abbreviated as LSBAM, (B0 for x = 0.00, B1 for x = 0.01, B3 for x = 0.03, B5 for x = 0.05 and B7 for x = 0.07) and pure LAO were prepared by auto combustion synthesis using the following chemicals: La $(NO_3)_3.6H_2O$ (John Baker, 99.5%), Sr $(NO_3)_2$ (Alfa Aesar, 99%), Al $(NO_3)_3.6H_2O$ (Alfa Aesar, 98%), Ba $(NO_3)_2$ (Alfa Aesar, 99%), and Mg $(NO_3)_2.6H_2O$ (Alfa Aesar, 98%) as a precursors and $C_6H_8O_7.H_2O$ (Emplura, 99%) as a fuel. The details of the sample preparation have been mentioned in chapter 2.

The structural phase of these samples was analyzed using Rigaku Miniflex II desktop XRD employing Cu-K_α radiation and Ni filter. The density of prepared sintered pellet was measured using the density kit (Sartorius, BSA2245CW). The grain and grain boundary morphology of sintered pellet was characterized using field emission scanning electron microscopy (FESEM; QUANTA 200 F). The elemental and chemical composition of the surface of theses was investigated using X-ray photoelectron spectroscopy (XPS) with Mg Kα beam. The electrical measurements were done using an LCR meter (Wayne Kerr 6500P) in the temperature range 100-700 ºC over the frequency range of between 20 Hz and 1 MHz.

4.4 Results and Discussion

4.4.1 Phase Identification using XRD

The phase evolution of LSBAM system was monitored by the XRD pattern and shown in the Fig. 4.2. The XRD pattern contains no impurity / secondary phase up to x = 0.03. The XRD peaks were indexed on the basis of trigonal (rhombohedral) perovskite structure with space group R-3c using JCPDS file no. 82-0478 [32]. It is observed that for

x > 0.03 the secondary phases of barium oxides BaO and BaO_2 develop. With a further substitution of Ba not only the intensity of these secondary peaks increases sharply, but an extra peak of $BaO_{1.3}$ also appears.

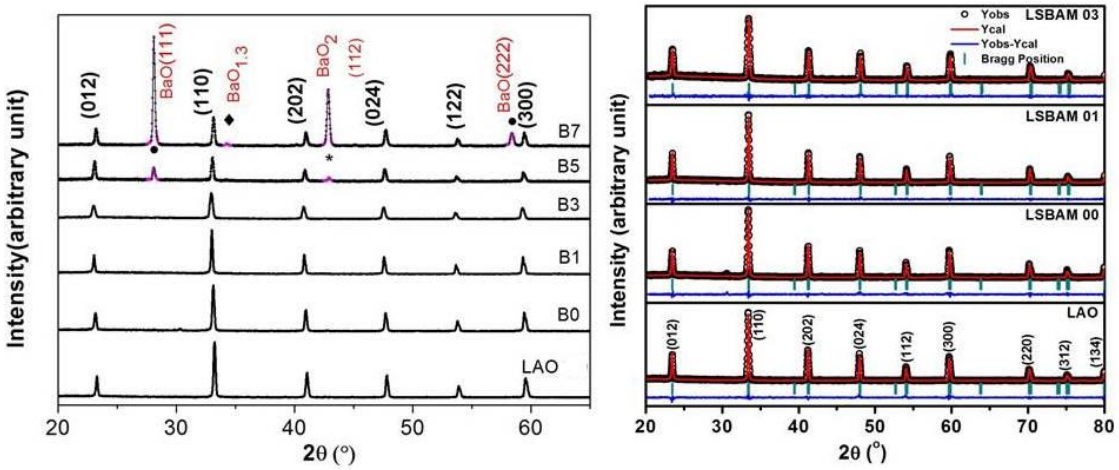

Figure 4.2: XRD pattern of Ba modified $La_{0.9}Sr_{0.1}Al_{0.9}Mg_{0.1}O_{3-\delta}$ (LSAM)

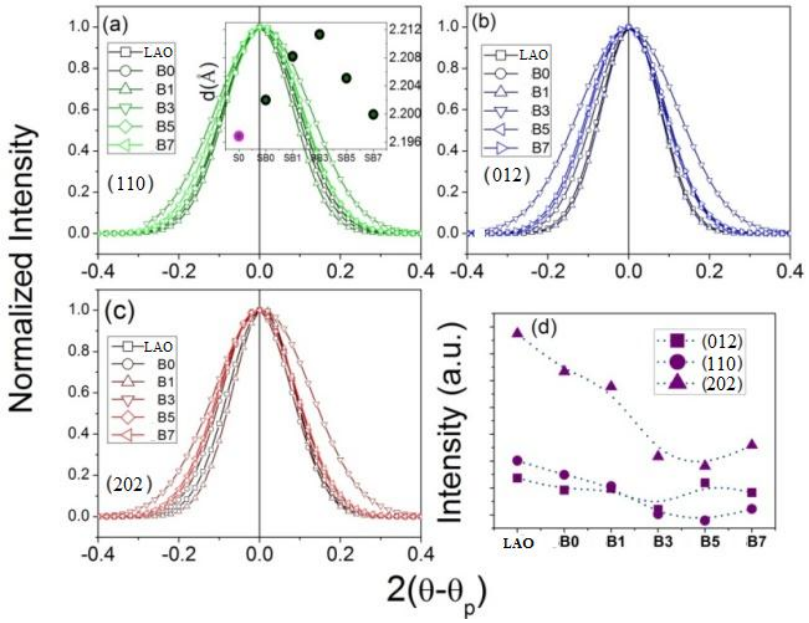

Figure 4.3: (a-c) Peak broadening and **(d)** Intensity variation for (202), (012) and (110) peaks respectively

Fig. 4.3 depicts the asymmetry and intensity variation of XRD peaks (202), (012) and (110) for all the studied samples. We observed that the highest broadening is for x = 0.03 for all the three peaks. The highest asymmetry in the peaks is observed for x = 0.01. Further, the intensity of the XRD peak shows a systematic decrease with x up to x = 0.03;

thereafter, it saturates. So, we can say that the percentage optimum value of Ba doping is 3% i.e., x = 0.03. Thus, further studies for sample having x > 0.03 were not carried out.

4.4.2 Compositional Details and Estimation of Oxygen Vacancy

Before the detail analysis of data, it was necessary to study about the elemental composition of the sample and its distribution. For this, EDX measurement was carried out. We were concentrated to Oxygen and Barium element. The atomic % of Barium (left top inset of Fig. 4.4) is slightly overestimated to 2 % (instead of 1%) and 5% (instead of 3%) which is acceptable within the limit accuracy of EDX and low concentration of Barium. But it is sufficient to conclude that barium is incorporated into lattice in the desired way. The atomic % of Oxygen (right bottom inset of Fig. 4.4) for various compositions were calculated. Further, deficiency of Oxygen was estimated and plotted in Fig. 4.4. The maximum deficiency is found for x = 0.03. Thus, there should be maximum oxygen vacancy and hence the ionic conductivity for x = 0.03.

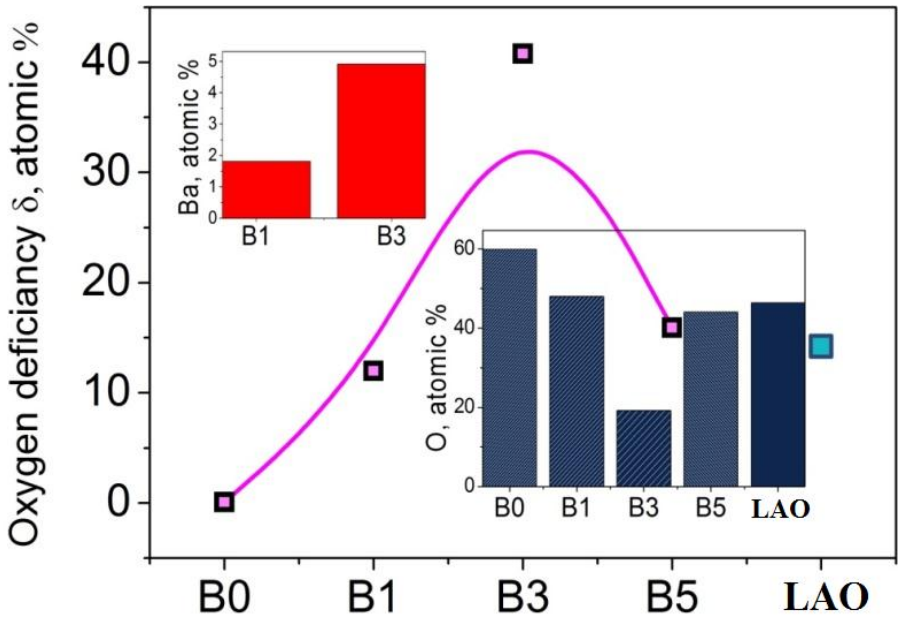

Figure 4.4: Oxygen deficiency estimated from EDX; inset: (right bottom) shows atomic % of O; (left top) shows atomic % of Ba) in Ba modified $La_{0.9}Sr_{0.1}Al_{0.9}Mg_{0.1}O_{3-\delta}$ (LSAM)

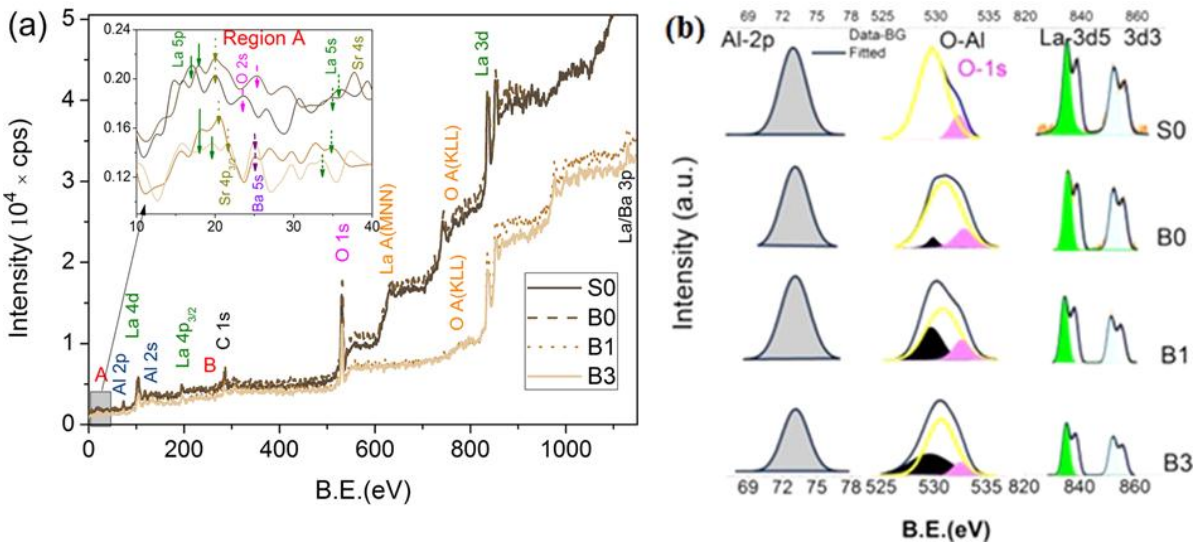

Figure 4.5: XPS spectra of Ba modified $La_{0.9}Sr_{0.1}Al_{0.9}Mg_{0.1}O_{3-\delta}$ (LSAM)

To analyze the constituent elements in details, the XPS spectra of the samples in the single phase, i.e., up to x = 0.03 were analyzed after calibration with C 1s peak at 284.6 eV. The intense photoelectric peaks are observed for La 3d, O 1s, La 4d, La 4p and Al 2p. Besides these peaks, some auger peaks corresponding to O (KLL) and La (MNN), are also observed, but with Ba substitution these auger peaks disappear. In order to check the presence of substituted element Mg, Sr and Ba, the spectra has been carefully observed and 'region A' has been shown in the inset of Fig. 4.5(a). In the 'region B', the presence of Sr-3p and La-4s electronic states is observed. For Mg, both possible electronic state, i.e., 2s and 2p are present, but the simultaneous presence of Ba-4d doublet, no particular trend can be observed. For Ba substitution, besides 4d state, a peak (Ba-5s) is also observed at ~ 25eV showing higher oxidation state. For Sr, the peaks corresponding to $4p_{3/2,}$ $3p_{1/2}$ and 4s are observed. As shown in Fig. 4.5 (a) (inset), with Ba substitution the peak $4p_{1/2}$ get broader and it does not shift, although its position is at 285 eV (4 eV higher). For La, almost all possible states are present with Sr and Ba substitution most of them shift towards higher B.E. and hence higher oxidation state. As La, Al and O are present in major ratio, thus most intense peak of these elements can give

insight of the materials. For these the spectra of al-2p, O-1s and La-3d for each sample were de-convoluted and plotted (Fig. 4 5b). In this figure, no significant variation with Sr and Ba substitution is observed for Al-2p (~ 73 eV) and La-3d (835 and 852 eV) doublet. A sharper peak of oxygen (O 1s) is de-convoluted at ~532 eV (O 1s) and ~530 eV (Al-O lattice) for S0 sample. With substitution a new phase at lower B.E. ~529 eV is observed to be evolving and a peak at 532 eV is found to reduce. This indicates a reduction of Oxygen and therefore may be linked to formation of Oxygen vacancy; which is maximum for x =0.03 samples. This finding is in correlation with the EDX analysis.

4.4.3 Rietveld and Structural Analysis

The XRD data of LAO, B0, B1 and B3 samples were analyzed using full prof Rietveld refinement. It is observed that the entire single phase XRD pattern can be easily fitted with R-3c symmetry. The value of refinement parameters is in the acceptable range. The variation of lattice parameters, bond angle and bond length with respect to tolerance factor has been compared (Fig. 4.6 (a-b)).

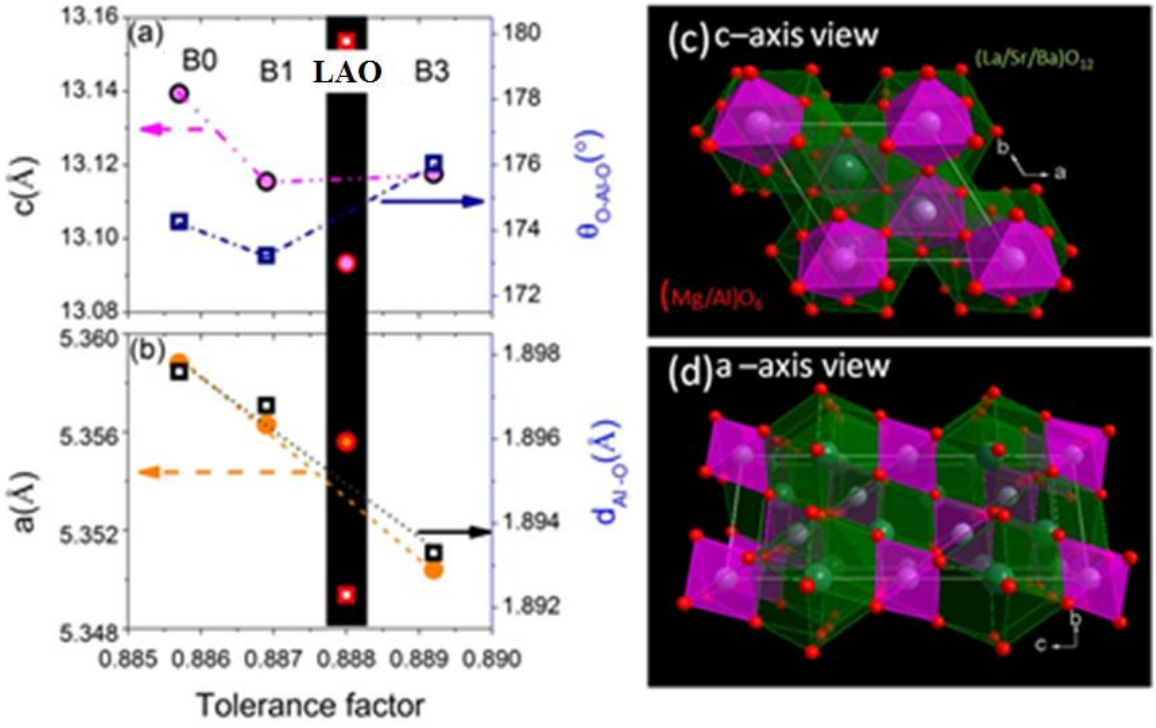

Figure 4.6: (a-b) Variation of Lattice parameters of Ba modified $La_{0.9}Sr_{0.1}Al_{0.9}Mg_{0.1}O_{3-\delta}$ (LSAM)

From this figure, It is observed that the lattice parameter ‘a’ and bond length Al-O decrease with the substitution of ‘Ba’ concentration and tolerance factor; while lattice parameter ‘c’ does not show any trend with tolerance factor, however, it is in correlation with Al-O-Al bond angle. This behavior can easily be understood after analyzing the structure of the system as shown in Fig. 4.6 (c-d). Fig. 4.6 (c) describes the c - axis view, there is enough space along a-axis and b-axis and hence the lattice parameter ‘a’ has a linear variation with tolerance. Fig. 4.6 (d) that describe the a-axis view shows that space along c-axis is occupied by both A-site polyhedron and B-site octahedron alternatively. A-site substitution with larger size cations makes a more compact situation. Thus, in order to get stable structure entropy of system, decrease by changing the bond angle. With more substitution, more oxygen vacancies should be created as suggested by EDX (on the fractured surface) and XPS results. The more oxygen vacancies will further facilitate relaxation in the bond angle. This makes, variation of lattice parameter ‘c’ is in correlation with bond angle instead of bond length.

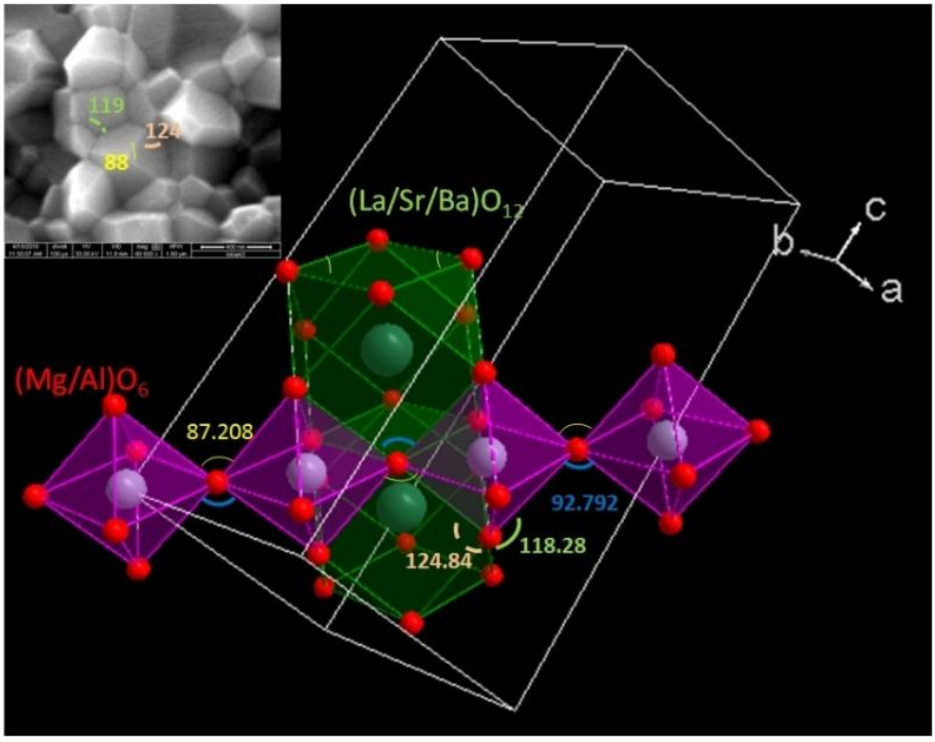

Figure 4.7: Angular correlation between the grains and lattice unit cell

4.4.4 Angular Correlation Between Grain and Lattice Structure

The angular correlation between the grains morphology and lattice unit cell is appearing as it can be seen in Fig. 4.7 indicates the very dense grain formation. The relative density of this system is calculated using Archimedes method. It is found to be in between 92-95%, which can be considered dense enough for an electrolyte system. Further grains are continuous, thus bricks layer model can be assumed in the system. The angular correlation is so strong that void between connecting grains are minimized; hence the easy path may be available for conduction along the grain boundaries.

4.5 Electrical Study

In general, in bulk sample, electro neutrality leads to Nernst -Einstein (NE) equation. In the absence of concentration gradient, NE equation further leads to the ohms law, i.e., $\vec{j} = -\sigma\overrightarrow{E}$ where $\sigma = F^2 \sum c_i u_i z_i^2$ is conductivity (with other notation F - Faraday constant, c – concentration, u- mobility and z- number of charge for i_{th} species). The correlation among concentration, type of charge species and conductivity enables the structural properties to be correlated with electrical properties. In the present system, as discussed earlier, the only active ionic species are O_2^- ion and further the ionic conductivity at higher temperatures is directly related to the creation of oxygen vacancies in these substituted perovskite materials.

Impedance spectroscopy (IS) is used as characterization of the electrical behavior of electrolytes as it can not only distinguish grain, grain boundary, and electrode contribution but also allows identifying the conduction mechanism. Typically, for ionic conduction in solid, high frequency data is required for measurement of associated time constant (usually in the range of 10^{-6} to 10^{-3}s). The motion of oxygen ion, which is in fact the much heavier ion as compared to electron will cease at high frequency beyond a few

MHz. Thus, IS has been carried out for a frequency range of 20 Hz to 1M Hz and corresponding Nyquist plots, for samples LAO, B0, B1 and B3 has been plotted at 600 °C and shown in Fig. 4.8 (a) (inset). However, in order to clarify the effect of substitution, the Nyquist plots on log-log scale are also re-plotted (Fig. 4.8 (a)). It is observed that with the substitution of Ba, the resistance of the sample decreases significantly. The grain boundary appears to be dominating in the whole spectra, as grain boundary resistance (R_{gb}) > grain resistance (R_g). With an increase in the temperature, R_{gb} as well as total resistance (R_t) decreases for all the samples shown in Fig. 4.8 (b) for B3 sample. In other words, we can say that with the substitution and temperature, the conductivity ($\sigma_t \approx \sigma_{gb}$) increases. The conductivity increases either due to temperature because of polarized or orientational charge species contributing to ionic character or due to the generation of another type of charge species. To identify the conduction mechanism, the conductivity spectra are described in terms of Jonscher power law (Fig. 4.8 (c) inset) and the parameters, i.e., dc conductivity (σ_{dc}), hopping frequency (σ_h) and exponent (n) is extracted. The hopping frequency has been used as a scaling parameter for Ghosh scaling mechanism. It is observed in Fig. 4.8 (c) that the scaling could not be achieved at high frequency showing the participation of heavy charge carriers, i.e. O^{2-} in the conduction mechanism and hence oxide ion conduction.

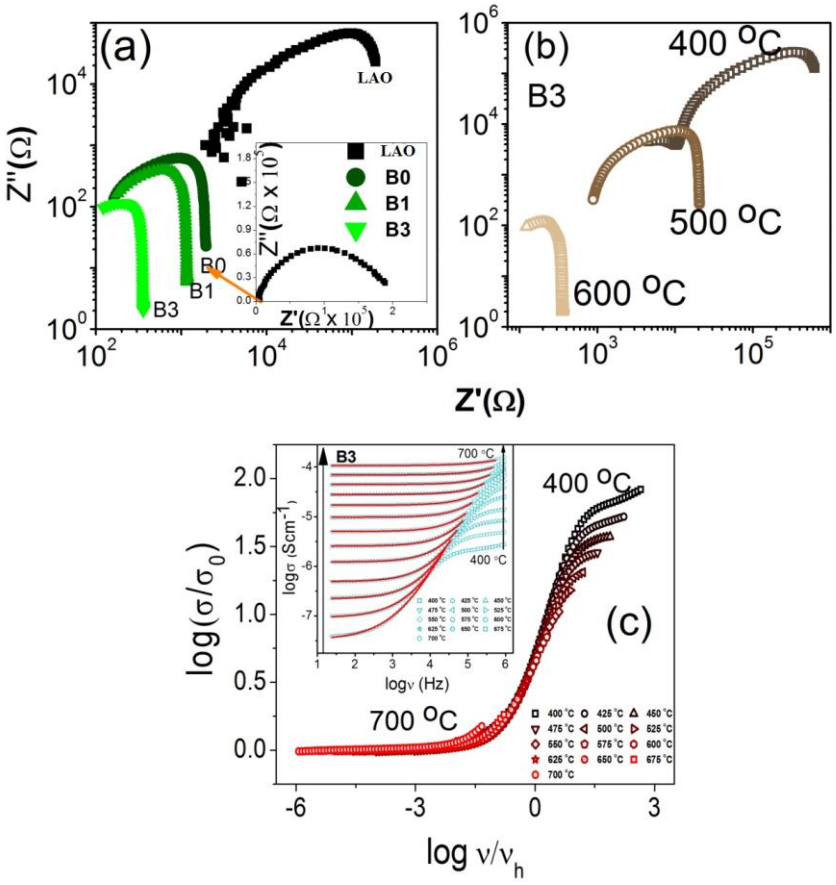

Figure 4.8: (a) log log Impedance Nyquist plots of Ba modified $La_{0.9}Sr_{0.1}Al_{0.9}Mg_{0.1}O_{3-\delta}$ (LSAM) at 600 °C.(inset) show normal Nyquist plot unable to resolve **(b)** Impedance Nyquist plots of B3 at 400, 500, and 600°C, **(c)** Scaling of conductivity (inset: Jonscher power law fitting)

4.6 Structure-Conductivity Correlation

In order to relate the conductivity data to the structure, the critical triangle for ABO_3 type perovskite materials (as illustrated in Fig. 4.9) were analyzed, as the size of A-site cation decides, whether it will allow the large size anion to pass through its lattice or not. It is observed that two other critical parameters the vertex angle α (A-B-A/B-A-B angle) and isosceles angle β (A-A-B/B-B-A) are in correlation to dc conductivity (σ_o) and grain boundary conductivity ($\sigma_g \approx \sigma_t$), respectively. However, there is exception for dc conductivity of LAO. Simultaneously, there is an increase in dc conductivity of B3 sample, whereas the grain conductivity of B3 is found to be slightly lower than B1.

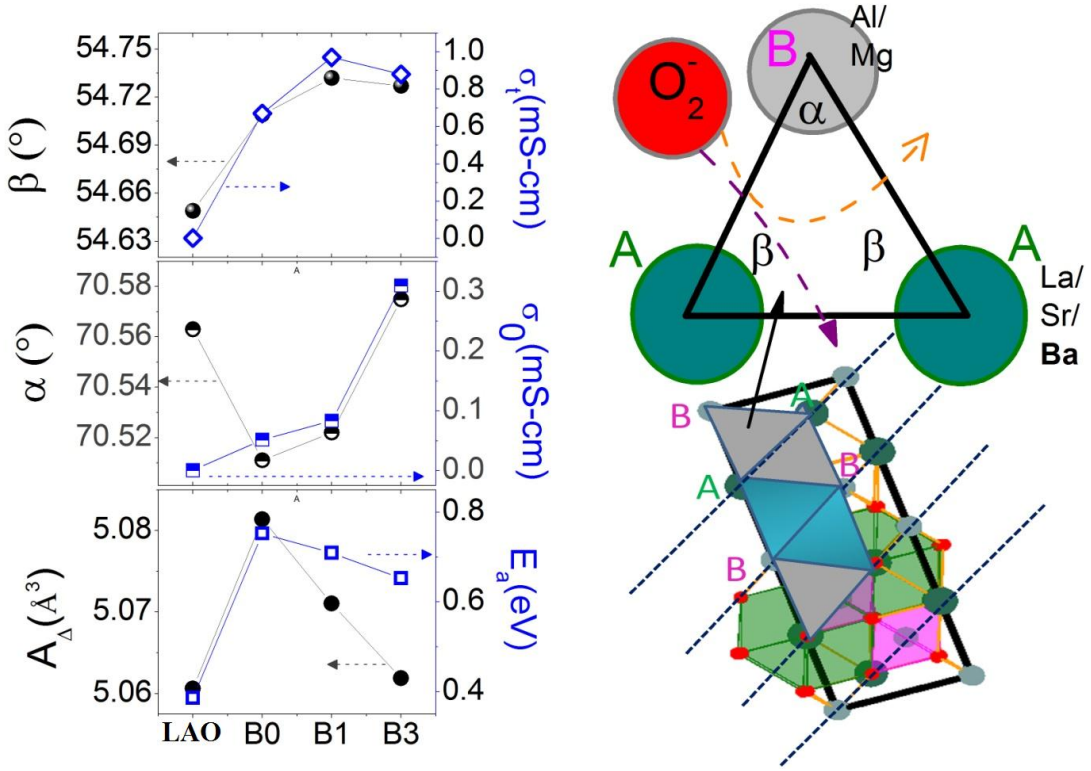

Figure 4.9: Correlation between the critical triangle structural parameter and the electrical parameters of Ba modified $La_{0.9}Sr_{0.1}Al_{0.9}Mg_{0.1}O_{3-\delta}$ (abbreviation: B0 for 0%, B1 for 1%, B3 for 3%, substituted Ba respectively and LAO for $LaAlO_3$

Further from Jonscher power fitting, the dc conductivity (σ_o) has been estimated and the dc conductivity data is found to best fitted for nearest neighbor hopping (NNH) (figure not shown). The activation energy is estimated from Arrhenius fitting for NNH conductivity. The activation energy is found to be around ~0.97 eV for LAO sample but in others substituted sample, it is in the range of 1.27-1.47 eV. This indicates the presence of doubly ionized oxygen vacancies. It is observed that the area of this critical triangle, $(l^2_{AA}/4)\tan\beta$ ($\equiv A_\Delta$) is related to the activation energy.

The mechanism can be understood in term of ionic radii (r_i) and length of sides of a critical triangle (l_{ij}). The ionic radii for 'Ba', 'Sr' and 'La' with 12 co-ordination number are 1.61 Å, 1.44 Å and 1.36 Å, respectively. It is noticeable that both 'Ba' and 'Sr'are s-block element and s-electron has a spherical electronic cloud. At the B-site, there is 'Al' and 'Mg' with ionic radii 0.535 Å and 0.72 Å for 6 co-ordination number, respectively. It

is well known that ionic radii of O_2^- is 1.4 Å with 6 co-ordination number. Now O^{2-} to move through the critical triangle, it is necessary that $\Delta_{ij} \equiv l_{ij}-(r_i+r_j)$ should be greater than $2r_0$, where i, j is a suffix for either of A, B. The value of the $l_{AA} = l_{BB}$ is 3.7846 Å, 3.7905 Å, 3.7870 Å, 3.7844 Å respectively for S0, B0, B1 and B3 sample. Now, even in the most favorable condition, i.e., Al at B-site, Δ_{BB} = 2.7205$\not>$2.8 Å but it is very close to $2r_0$. Thus, in dynamic conditions, it is possible that O^{2-} can pass through sides of critical triangle. Also, with the increase in temperature Δ_{BB} approaches to 2.8 Å as temperature dependent XRD reveals lattice expansion with temperature. So, O^{2-} can move through B-B lattice. But it cannot move through A-A lattice side as, Δ_{AA} = 2.0705 $\not>$ 2.8 Å. Also, the cross sectional area of O^{2-} is πr_0^2 = 6.16 $Å^2$ which is less than void in between ABAB-parallelogram with area $(l^2_{AA}/4)\ \tan\beta = 2A_\Delta$ = 10.09 $Å^2$. Therefore, we can assume that there is a possibility of oxygen ion movement through A-B lattice as shown in Fig. 4.10. This kind of movement resembles with Holstein like NNH hopping. The electrical conductivity results also suggest NNH mechanism. Thus, there should be a correlation between structural parameter and electrical conductivity.

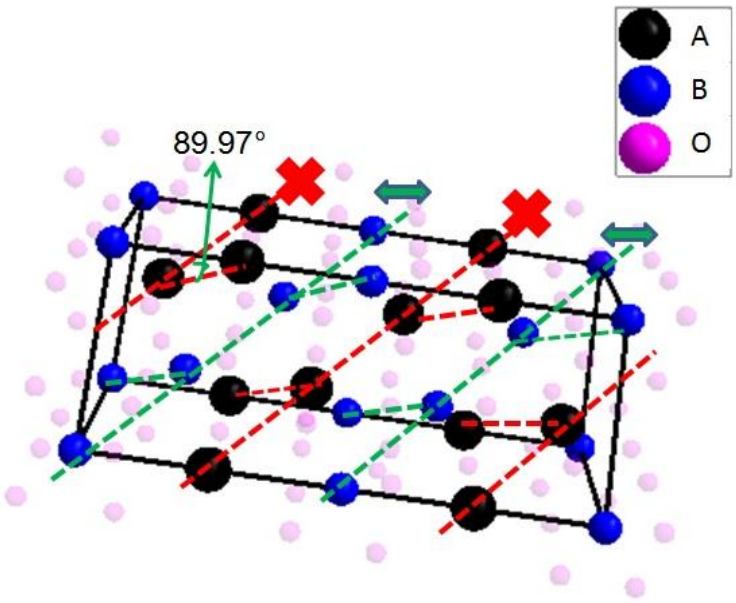

Figure 4.10: Migration path for ionic conduction of oxygen ion has been mapped out using the correlation of bulk conductivity with A-A-B angle (β) and of dc conductivity with A-B-A angle (α)

The effect of substitution is clearly reflected in the results and can be understood as follows. Firstly, with co-substitution (with 10% by mole) of Sr^{2+} and Mg^{2+} ions, the grain conductivity increases sharply in comparison to a small increase in the dc conductivity (Fig. 4.9). Also, the area of critical triangle significantly increases. It can be also seen that the lattice expansion with co-substitution is clearly evident and, therefore the easy passes for O^{2-}. Thus the ionic conductivity should increases as compare to S0 sample. Now, with double substitution at A-site by Ba (larger ionic radii among these ions), the lattice parameter decreases along with a small rise in the value of β. It leads to reduced area of the critical triangle and hence hindrance to O^{2-} movement. With the further increase in Ba content, the value of α and dc conductivity increases sharply. Apart from α, the other parameters i.e., β and area of the critical triangle have reduced and block the passage of O^{2-}. Hence, the increase in dc conductivity is not due to O^{2-} or in other words it is not ionic. Another critical triangle parameter is α angle. The small value of α means greater intra-atomic interaction. In case of S0, where only La^{+3} is present at A-site, the correlation could not be established as La^{+3} does not possess outer most shell (d) electron. Therefore, electronic conductivity is much reduced than expected from the critical triangle analysis. The increase in dc conductivity for B3 is clearly due to the charge neutrality condition that is followed for this sample. Only electrons can move in this case through the critical triangle. It also supports the observation of possible polaronic conduction in B3 sample due to most diffusive XRD peaks. The variation of dc conductivity with temperature (up to 1000K) is shown in Fig. 4.11 (a). The data are well fitted ($r^2 > 0{:}996$) with space charge ionic model ($\sigma = {}^{A}{}_{1}/T \exp({}^{A}{}_{2}/T)$). The polynomial expansion of model gives an alternating series hinting for bosonic contribution instead of fermionic contribution. It is noticeable that O^{2-} is boson while, the electron is fermions. Also, the activation energy estimated for these samples was found to be 0.97, 1.47, 1.35

and 1.27 (in eV) respectively this indicates doubly ionized oxygen vacancy as reported earlier. Thus, in these samples the ionic conductivity dominates.

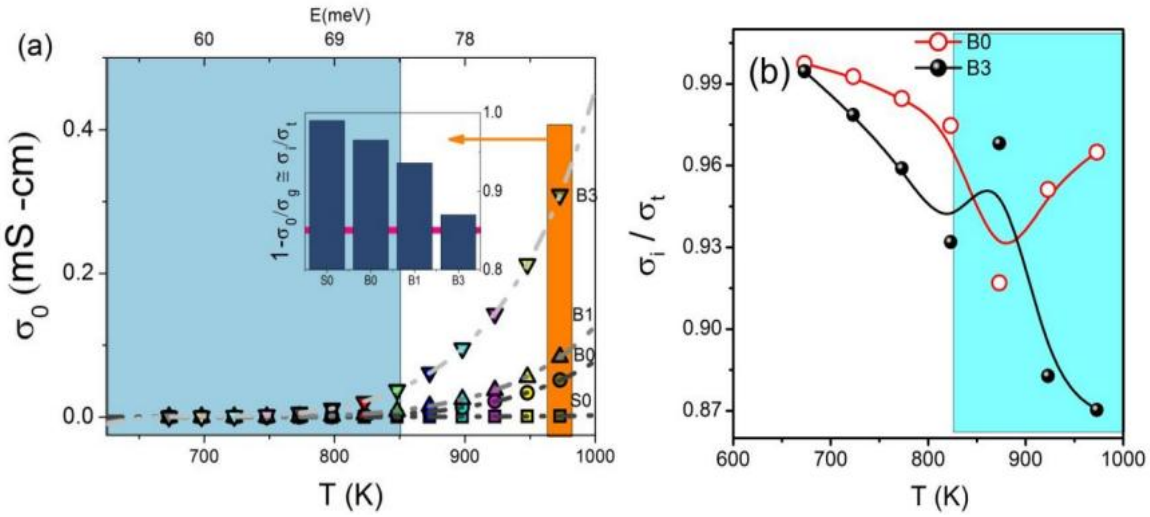

Figure 4.11: (a) DC conductivity of Ba modified $La_{0.9}Sr_{0.1}Al_{0.9}Mg_{0.1}O_{3-\delta}$ (abbreviation: B0 for 0%, B1 for 1%, B3 for 3%, substituted Ba respectively and S0 for $LaAlO_3$ (Inset) shows the relative ratio of ionic conductivity to total conductivity at 973K **(b)** Shows variation of the ratio with temperature

The variation of dc conductivity with temperature (up to 1000 K) is shown in Fig. 4.11 (a). There is a systematic increase in conductivity with co-substitution and double- substitution, as indicated by vertical bars at 973 K. It is highest for 3% Ba double substituted $La_{0.9}Sr_{0.1}Al_{0.9}Mg_{0.1}O_{3-\delta}$. Though conductivity increases, but it appears that double substituted samples possess more electronic contribution as it rises sharply once thermal energy reaches 75 meV. This fact is further supported from the decrease in the activation energy obtained from space charge ionic model (though overall, conduction is highly ionic in nature). The value of thermal energy corresponds to activation energy associated with polaronic conduction. To support this fact, we calculated the transport number, the ratio of ionic conductivity to total conductivity. In this calculation, we assumed that the difference between bulk conductivity and dc conductivity is due to oxide ion conduction and hence the conductivity is ionic in nature. The transport number calculated for LAO is well in accordance with the literature. The transport number has

been calculated for co- and double- substituted samples and shown by bar chart (Fig. 4.11 (a), inset). This clearly reveals that though total conductivity as well as ionic conductivity increases with co- and double substitution, but at the same time there is an increase in electronic conductivity, which is reflected by decreasing nature of transport number. In order to compare, the variation in the transport number with temperature is shown for the B0 and B3 in Fig. 4.11 (b). It clearly indicates that the ionic conduction is sharply decreasing in case of B3 accept the fluctuation around the zone boundary transition (~830 K). It also supports the rise in polaronic conduction in B3 sample. Therefore, in spite of having a better value of conductivity, the B3 is not better choice of electrolyte material. Thus, we purpose an insight mechanism how A-site alio-valent substitution can alter effective ionic radii and hence its electrical properties. This mechanism easily explains why Ca ($r_{Ca2+} \approx 1{:}34$ Å is slightly less than $r_{La3+} \approx 1{:}36$ Å) substituted LAO is better ionic conductor and always show high transport number > 0.9 as compared to 'Ba' substituted LAO.

4.7 Chemical and Thermal Stability

The chemical stability in the presence of the fuel and thermal stability of the electrolyte materials is necessary. In order to verify it, B0 sample is kept in Ethanol (C_2H_5OH) for long duration of time of one month (Fig. 4.12 (a)). The comparative XRD pattern of B0, with and without ethanol is similar with no signature of degradation at all. It indicates the sample is chemically stable. For thermal stability, the XRD measurement was made up to 700 °C temperatures (Fig. 4.12 (b)). There is no signature of degradation observed from the XRD pattern with temperature. This indicates the sample is both thermally and chemically stable.

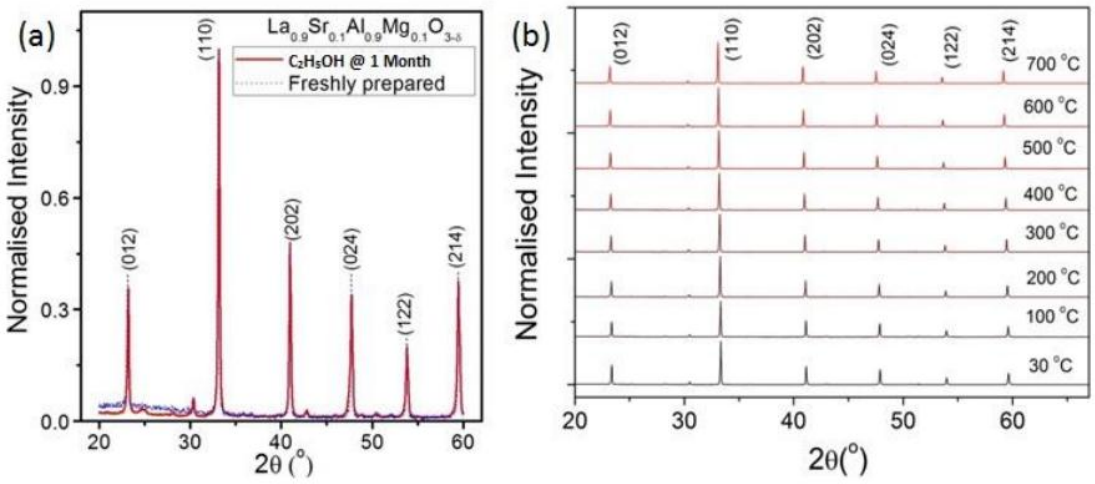

Figure 4.12: Comparative XRD of sample $La_{0.9}Sr_{0.1}Al_{0.9}Mg_{0.1}O_{3-\delta}$ **(a)** Freshly prepared sample and sample kept in ethanol for one month **(b)** At different temperatures

PART B

Synthesis of the Sample $(La_{0.89}Ba_{0.01})Sr_{0.1}Al_{0.9}Mg_{0.1}O_{3-\delta}$, B1 by Tape Casting Technique and Analysis its Structural and Electrical Properties

As discussed above about the alio-valent double substitution of Ba on A-site of $La_{0.1}Sr_{0.1}Al_{0.9}Mg_{0.1}O_{3-\delta}$, (LSAM). Since prime requisite of electrolyte system is that it should be high oxide ion conductivity. For this, electrolyte should be as thin as possible so that the ohmic loss is reduced. Therefore, tape casting of the electrolyte in the form of thin tape is essential. For this purpose, it has been chosen only the system $(La_{0.89}Ba_{0.01})Sr_{0.1}Al_{0.9}Mg_{0.1}O_{3-\delta}$, B1, out of the above mentioned double substituted Ba series samples like LAO, B0, and B3. Further, we have compared the structural and electrical properties of both the pellet and the tape synthesized. Synthesis of both the tape and the pellet powder was same mentioned in chapter 2. The process of sintering for the tape and pellet is shown in Fig. 4.13.

Figure 4.13: Comparison of synthesis techniques of the tape and the pellet of B1 sample

4.8 Structural Studies

Fig. 4.14 (a) shows the XRD patterns of the sintered tape and sintered pellet, which matches well with the pervoskite $LaAlO_3$ structure.

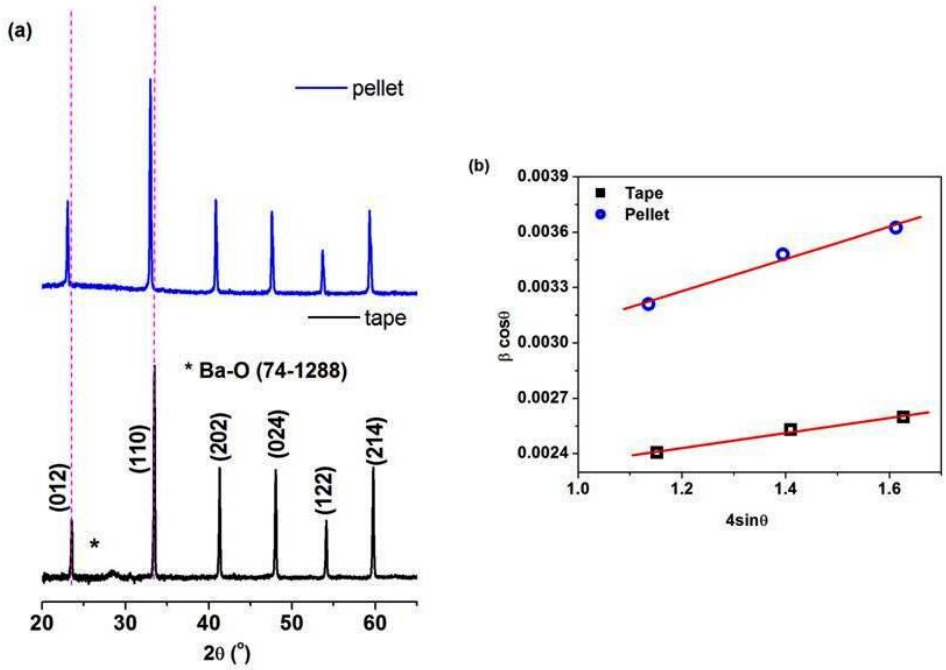

Figure 4.14: Structural analysis of tape and pellet of B1

All the diffraction peaks of sintered B1 tape are identified as the single phase of a rhombohedral perovskite structure with space group $R\bar{3}c$ using JCPDS file No. 82-0478. The lattice parameters of the pellet and tape are mentioned in Table 4.1. According to JCPDS file No.74-1228, the secondary phase observed is Ba-O in sintered tape i.e. in tape Ba has not taken appropriate place in the lattice. Whereas, no secondary phase is observed in sintered pellet. It can also be seen that the XRD peaks corresponding to $2\theta \approx 22^{o}$ and 32^{o} of a sintered pellet shift toward left in comparison to sintered tape. Hence, the lattice parameters have increased in the pellet in comparison to tape casted sample. The microstrain and crystallite size have been calculated from XRD results by using the Williamson-Hall model [82]. The Williamson Hall-model is given by:

$$\beta \cos\theta = 0.9\frac{\lambda}{t} + 4 \in \sin\theta \qquad 4.1$$

where, *'t'* is average crystallite size, ϵ is microstrain, β is full width at half maxima (FWHM) at Bragg's angle (2θ) and λ being the X-ray wavelength of CuKα (λ = 1.54098 Å). The slope of $\beta\ cos\theta$ vs $4sin\theta$ curve (Fig. 4.14 (b)) gives the value of microstrain and intercept gives the value of crystallite size. Table 4.1 shows the variation of microstrain and crystallite size for both the tape casted and pellet samples. It is observed that microstrain in tape casted sample is higher than that of the pellet sample. The crystallite size obtained from W-H plot in tape casted sample is higher than that of pellet sample. The crystallite size corresponding to strongest peak (110) was calculated using Scherrer formula and found to be in accordance with the crystallite size calculated from W-H plot. Moreover, the specific surface area along the strongest plane is calculated using formula

$$\frac{6}{D \times \rho} \qquad 4.2$$

where, D and ρ are crystallite size and density of rhombohedral $LaAlO_3$ nanocrystals, respectively, and was found to be 375.7 × 10^6 cm^2/g. On comparison with the standard value (JCPDS file No. 82-0478), the surface area increases, which can be due to the high surface energy of the particles. It is well known that an increase in surface area increases the surface energy. The sintered pellet is denser than sintered tape as density of sintered tape was measured to be 4.6 gm/cm^3 whereas density of sintered pellet was found to be 5.8 gm/cm^3 (Table 4.1). The density of tape is about 75.4% of theoretical density.

Table 4.1: Lattice parameters of both the pellet and the tape

Table 4.1					
Samples	**Lattice Parameters (Å)**	**Density (g/cm^3) d_{th} =6.3**	**DC conductivity at 700 °C (Scm^{-1})**	**Crystallite size (nm)**	**Microstrain (ϵ)**
Tape	a=5.34614 c=13.1881	d_{ex}=4.6	6.0×10^{-4}	71.94	3.299 X 10^{-4}
Pellet	a=5.4222 c=12.0098	d_{ex}=5.8	4.64×10^{-2}	62.18	8.729 X 10^{-4}

4.9 Microstructural Studies

The SEM micrographs of homogeneous B1 tape and pellet are shown in Fig. 4.15 (a) and Fig. 4.15 (b), respectively. Fig. 4.15 (a) depicts that crystallite growth is homogeneously distributed over the entire area in both sintered tape and pellet. It can be seen that the grains are distributed non-uniformly having broad size distribution. This is due to the high surface energy of the particles as mentioned above. The tape casted sample having smaller grain sizes as shown in Fig.3 is characterized by low amounts of

microstrain. Fig. 4.15 (b) depicts the formation of dense hexagon grains in the pellet sample. Whereas in the tape, the grains formed are not hexagon in shape. This figure shows low connectivity in between grain and grain boundary. To further analyse the secondary phases observed in X-ray Diffractograms, EDAX measurements have been done for both the sintered tape and pellet at the grain and grain boundaries shown in Fig. 4.15 (c) and Fig. 4.15 (d). Fig. 4.15 (e) depicts the elemental constituents of the sintered tape and pellet. It is observed that in sintered tape, Ba is nearly absent than in sintered pellet showing that Ba has not entered the lattice in sintered tape as Ba content is absent in grains but present in the grain boundaries (graph not shown here). It is also observed in Fig. 4.15 (e) that the oxygen content in sintered tape is more than that of the oxygen content in sintered pellet.

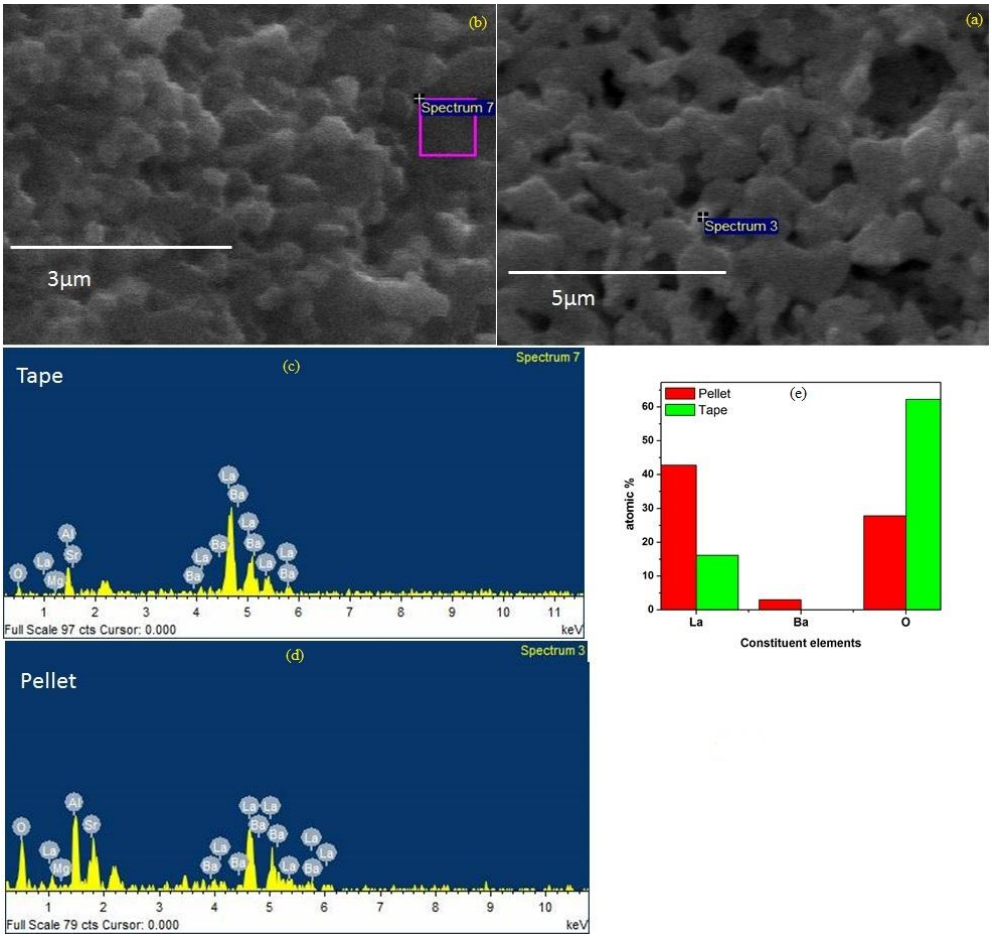

Figure 4.15: SEM and EDX measurement of pellet and tape of B1

4.10 Impedance Analysis

As structural and micro-structural studies indicate that in sintered tape, oxygen content is more and Ba is present at the grain boundaries or in secondary phases. Now the question arises, how the content of Ba or O will affect the conductivity of the tape and pellet.

The dielectric relaxation of a dielectric or semiconducting system usually consists of dipolar and conductivity relaxation mechanisms. In case of conductivity relaxation mechanisms, the dispersion in dielectric constant is determined through long-range charge carriers' diffusion and dielectric response is described through electric modulus and impedance. Hence, impedance formalism has been adopted to study the conductivity relaxation mechanism for both the samples.

The Impedance profile (Nyquist plot) from temperature 400 ^{o}C to 700 ^{o}C for the tape casted and pellet sample is shown in Fig. 4.16 (a) and Fig. 4.16 (b), respectively.

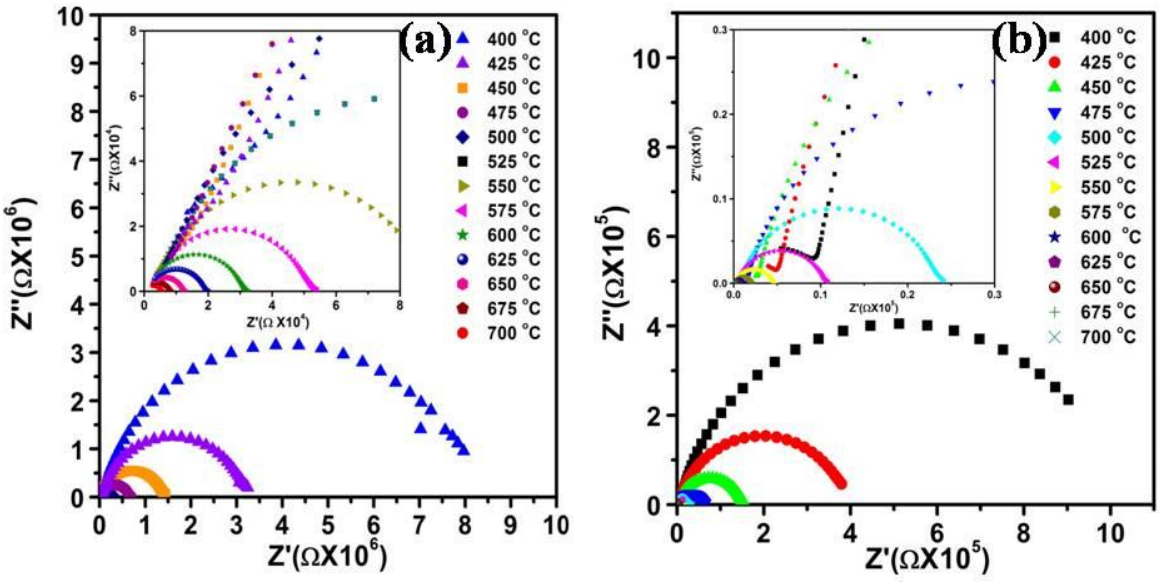

Figure 4.16: Nyquist plot of **(a)** Tape and **(b)** Pellet of B1

The impedance plot usually consists of three circular arcs, a small arc in the high frequency region passing through origin, the second arc in the intermediate frequency

region and third arc in the low frequency region. The intercept of the arcs on the real axis represents the contribution of grain, grain boundaries and electrode-specimen interface in the high frequency, intermediate frequency and low frequency regions, respectively. The values of the grain (bulk) resistance R_g, and grain boundary resistance (R_{gb}) can be determined from the intercepts of these semi-circular arcs on the real axis (Z'). In the tape casted sample, the arc in the low frequency region becomes more distinct with increasing temperature and at 700 ^oC it shows one resistance and one circular arc in the mid-frequency region. The arc corresponding to grain contribution disappears above 400 ^oC (Fig. 4.16 (a)) in tape casted sample. Whereas, in sintered pellet, the grain contribution is followed by a spike showing the conducting specimen and at 700 ^oC it shows nearly the same behavior as in sintered tape. Fig. 4.17 (a) and Fig. 4.17 (b) shows one resistance and one semi-ciruclar arc in the mid frequency region of the tape casted and pellet sample at 700 ^oC respectively. It is observed that the tape formed is more resistive than the grain boundary. In order to correlate the electrical properties of the tape casted sample and pellet with the microstructure of the material, an equivalent circuit consisting of one resistance and one parallel R-Q circuit connected in series has been used to interpret the nature of impedance plane plots as shown in Fig. 4.17 (a) and Fig. 4.17 (b). Here R and Q are the resistance and constant phase element for the semi-circular contributions. This is indicative of non-ideal behaviour of capacitance and occurrence of more than one relaxation processes with similar relaxation time.

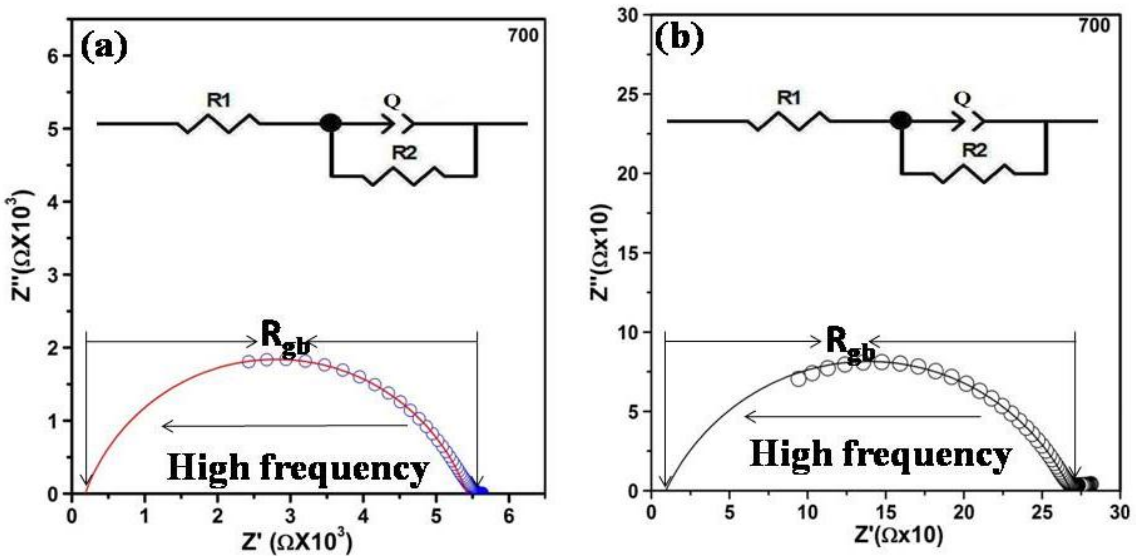

Figure 4.17: An equivalent circuit diagram of Nyquist plot **(a)** tape and **(b)** pellet

The capacitance of CPE is given by the relation $C = Q^K R^{(1-K)/K}$, where the parameter k estimates the deviation from ideal capacitive behavior [83]. The values of K are zero for the pure resistive case and unity for the pure capacitive one. The values of K, Q, R and C are mentioned in Table 4.2. The values of K are calculated from the slope of the corrected modulus, log|Z| *vs* log frequency plots (Fig.4.18).

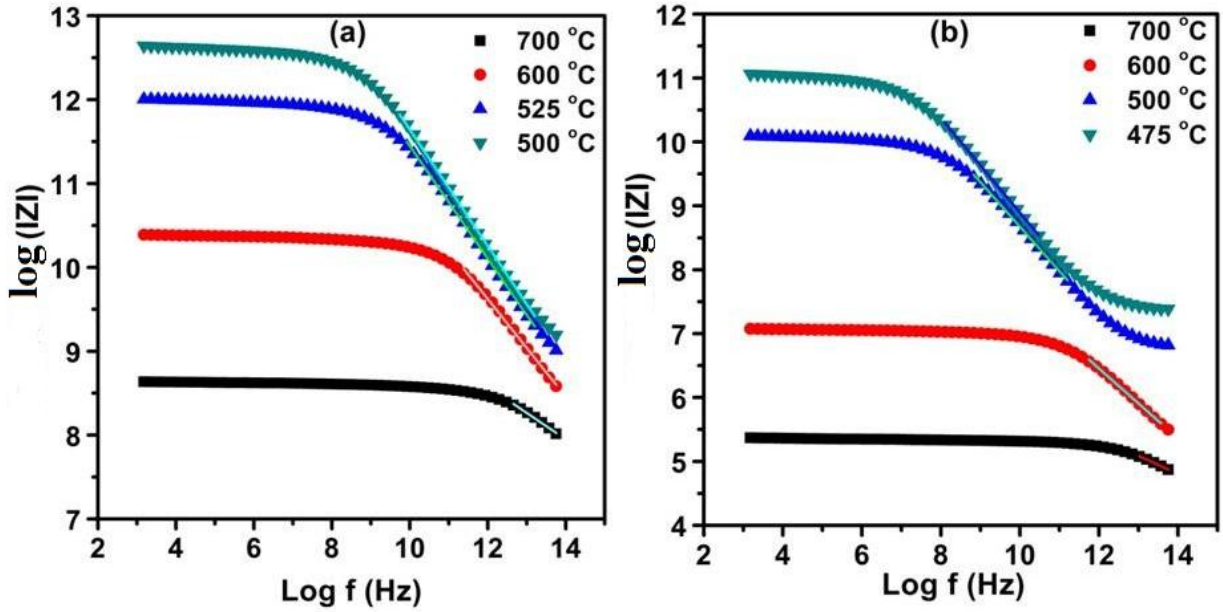

Figure 4.18: logIzI *vs* log f of **(a)** Tape and **(b)** Pellet

At high frequencies, the corrected modulus is dominated by the contribution of the imaginary part of the impedance. The corrected modulus approaches zero according to $|Z|_{adj} \approx f^{K}$ [84]. Thus, the slope on a logarithmic plot has a value of –K at high frequencies. It is observed that the value of K ranges from 0.7 to 0.2 with temperature from 400 ºC to 700 ºC in both the tape casted and pellet samples (Table 4.2).

Table 4.2: The values of K, Q, R and C for both the bulk and the tape

Table 4.2							
Tape	**Temperature (°C)**	**Frequency (Hz)**	**T(sec)**	**Q**	**R(Ω)**	**C**	**K**
	500	8203.73	1.9410E-05	6.7444E-11	287797	2.6955E-08	0.691
	525	17011.2	9.3606E-06	6.1073E-11	153270	2.6141E-08	0.678
	600	105329	1.5117E-06	5.1422E-11	29400	8.4149E-08	0.599
	700	652170	2.4416E-07	4.6307E-11	5272.7	3.2459	0.266
Pellet	**Temperature (°C)**	**Frequency (Hz)**	**T(sec)**	**Q**	**R(Ω)**	**C**	**K**
	475	1589.94	1.0015E-04	1.6556E-09	60492	2.4092E-07	0.704
	500	5697.03	2.7950E-05	1.2294E-09	22736	1.2654E-07	0.701
	600	126395	1.2598E-06	1.2486E-09	1009	1.2758E-06	0.524
	700	939125	1.6955E-07	9.7671E-10	173.6	0.4090	0.219

Usually, the value of K determines the roughness of the surface, but the surface roughness gives only the minute changes. But in the present case, K changes with the temperature, which can be attributed to the formation of ionic charge carriers in comparison to the deformation in the lattice [85]. This can be explained on the basis of the gradient of oxygen vacancies formed in the specimen as shown in EDAX graph that there is more oxygen in tape casted sample in comparison to pellet whereas, the value of K is larger in the pellet in comparison to tape but not a very large difference as can be

seen through Table 4.2. The small changes in the value of K from pellet to tape can be correlated to the deformation of the surface or surface roughness.

The total conductivity calculated from the intercept of the Nyquist plots on real axis of the sample is shown in Fig. 4.19 (a) in Arrhenius fashion. The activation energy (E_a) of the tape sample is calculated from the slope of the straight line and was found to be 0.63 eV whereas the activation energy for the pellet is high i.e. 0.76 eV. Further, the conductivity of the tape is much less than that of the pellet. The formation of less number of oxygen vacancies contributes to decrease in activation energy in sintered tape as more oxygen is observed in it. In addition, the lowering in conductivity of the tape may be due to the formation of Ba impurity that may accumulate at grain boundaries making it more insulating as shown in EDAX analysis. Moreover, the higher conductivity in the pellet can be attributed to the dense hexagon grains and high oxygen vacancies as shown through EDAX measurements.

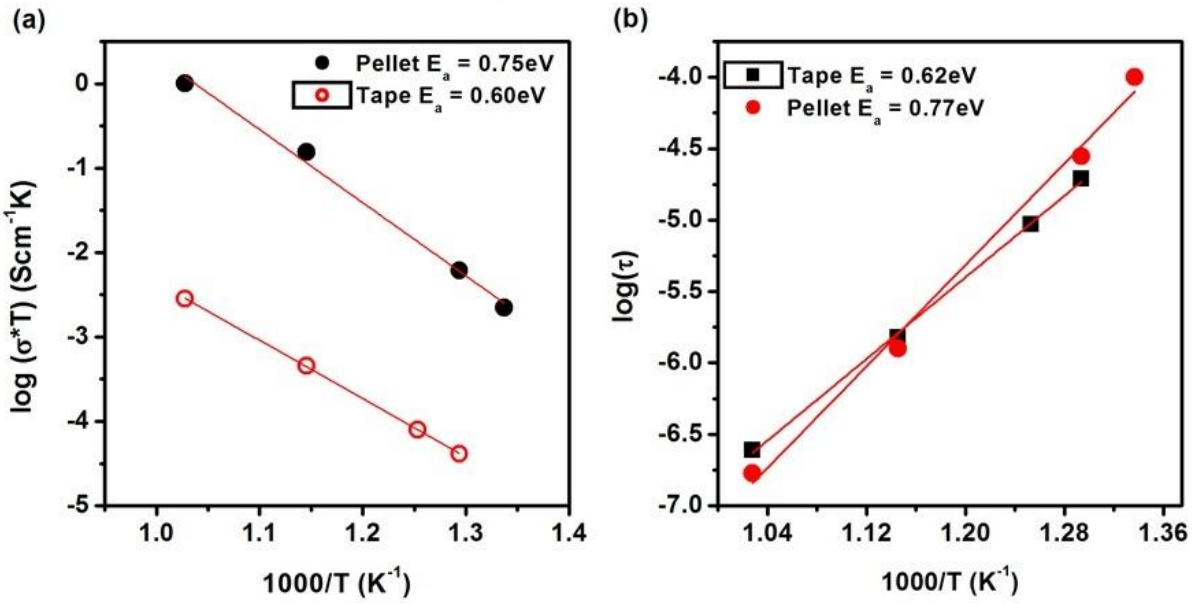

Figure 4.19: (a) log (σT) *vs* 1000/T **(b)** logτ *vs* 1000/T for activation energy

To further verify the activation energy and content of oxygen vacancies, the relaxation time calculated from Nyquist plots has been plotted with the inverse of temperature.

Fig. 4.19 (b) shows the variation of log τ *vs* 1000/T (K^{-1}). The activation energy obtained from the slope of the plot is in accordance with the value of activation energy obtained from the conductivity plots showing the formation of ionic charge carriers and vacancies illustrated in below equation.

$$2(0.1)MgO + 2(0.1)SrO + 2(0.01)BaO \xrightarrow{(0.1\,1)LaAlO_3} 2(0.1)Sr'_{La} + 2(0.01)Ba'_{La} + 2(0.1)Mg'_{Al} + (2+0.01)(0.1)V_O^{\bullet\bullet} + 2(2+0.01)(0.1)O_o$$

The amount of oxygen vacancies has been altered with the processing conditions, i.e. less number of oxygen vacancies are formed in tape sample in comparison to pellet sample.

4.11 AC Conductivity Analysis

To analyse the ion dynamics, conduction mechanism and to find out the reason for different activation energy in both the tape casted sample and pellet, AC conductivity has been studied. The log-log plot of frequency dependence of ac conductivity at various temperatures for both the tape and pellet is shown in Fig. 4.20 (a) and Fig. 4.20 (b), respectively. The data has been analysed with the Jonscher power law in Eq. 2.4. [86]–[88]. The exponent represents the electrical relaxation behaviour with the material. In Fig. 4.20 (a) and Fig. 4.20 (b), the symbols indicate the data points and the lines indicate the fitting according to Eq. 2.4. It is observed that the conductivity is independent at low frequencies and increases with the increasing frequency after a certain value. At higher frequencies, the conductivity exhibits dispersion, increasing in the form of power-law and tend to form another plateau in low temperature regime and then this plateau becomes

invisible in the high temperature regime. From the fitting of data with the Jonscher Power law, dc conductivity, exponent and hopping frequency have been calculated.

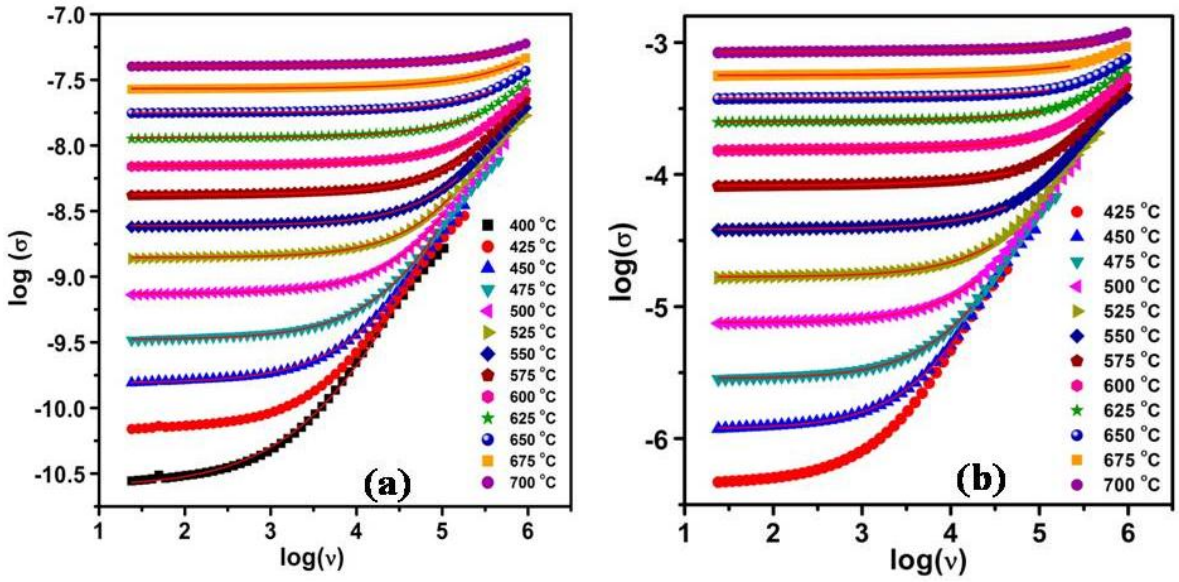

Figure 4.20: log (σ) vs log (ν) **(a)** Tape and **(b)** Pellet of B1

As discussed earlier that the value of K changes with the temperature showing the gradient of oxygen vacancies with the temperature. To verify this observation, various scaling mechanisms have been followed. Out of these mechanisms, the conductivity spectra has been scaled using Hopping frequency as a scaling parameter known as Ghosh scaling. It has already been proven that conductivity spectra follow the time temperature superposition principle, which states that conductivity isotherm can be superimposed on a single master curve using conductivity and frequency as the scaling parameters. The principle can be mathematically expressed in Eq. 2.6

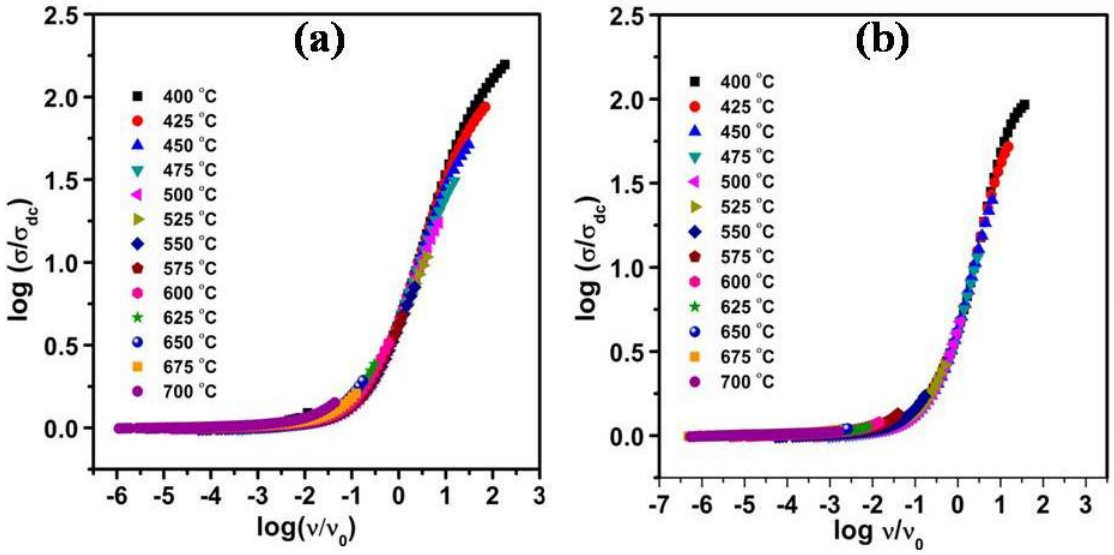

Figure 4.21: Variation of log (σ/σ_{dc}) vs log (ν/ν_0) for tape and pellet

Fig. 4.21 (a and b) shows the variation of $\log(\sigma/\sigma_{dc})$ vs $\log(\nu/\nu_o)$ for the tape casted and pellet specimen. It is observed in tape casted specimen that Ghosh scaling is not valid at higher frequencies whereas Ghosh scaling is valid for the pellet specimen. This shows that the conduction phenomenon is temeperature and frequency independent in pellet rather than in tape. In pellet, it can be said that with the change in temperature only the number of charge carriers is changing keeping the conduction mechanism invariant, whereas, in sintered tape, the number of charge carriers as well as the type of charge carriers are changing at high temperature and high frequencies, leading to the change in conduction mechanism [63].

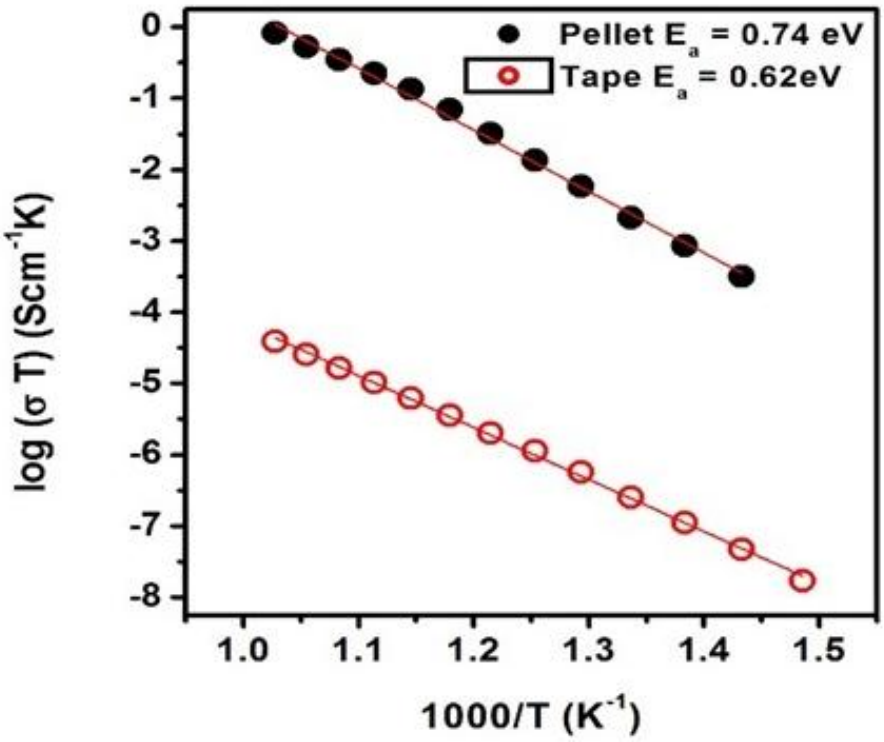

Figure 4.22: Arrhenius plot of tape and pellet

The activation energy has been calculated for the dc conductivity obtained from Jonscher power law fitting. Fig. 4.22 shows the variation $\log(\sigma_{dc}\ T)$ vs 1000/T for the tape and pellet respectively. The activation energy obtained is 0.63eV for tape and 0.74 eV for pellet respectively, which is in good agreement with the activation energy obtained from the total conductivity using Nyquist plots.

4.12 Conclusions

In summary, a systematic study on structural properties of Ba substituted $La_{0.9}Sr_{0.1}Al_{0.9}Mg_{0.1}O_{3-\delta}$ and its correlation with conductivity are carried out. It is observed that the value of conductivity can be better correlated with the critical triangle angle rather than the length of its sides. Consequently, A site substitution with and without B- site substitution, effectively controls the ionic conductivity. However, alio-valent acceptor double substitution at A site with larger ionic radii

decreases the oxide ionic conductivity and it may increase with smaller ionic radii acceptor substitution.

Also, It is concluded that B1 tape has been prepared by tape casting method using the Doctor's blade technique has lower conductivity than B1 pellet. The XRD pattern shows a rhombohedral perovskite structure with the shifting of peaks corresponding to $2\theta \sim 22^{o}$ or 32^{o}. The activation energy obtained from the conductivity calculated from Nyquist plots, conductivity from Jonscher power law fitting and relaxation time are in good agreement. The values of K in the range of 0.7-0.2 show the formation of ionic charge carriers and EDAX measurements confirms higher oxygen content in tape casted samples. The low conductivity of the tape could be because of less number of oxygen vacancies and accumulation of Ba impurity at the grain boundaries.